Journal of Applied Geophysics 149 (2018) 1–9

Contents lists available at ScienceDirect

Journal of Applied Geophysics

journal homepage: www.elsevier.com/locate/jappgeo

Three-dimensional magnetotelluric modeling in anisotropic media using edge-based finite element method

Tiaojie Xiao [a,b,*], Yun Liu [a], Yun Wang [a], Li-Yun Fu [a]

[a] Institute of Geochemistry, Chinese Academy of Sciences, Guiyang 550002, China
[b] University of Chinese Academy of Sciences, Beijing 100049, China

ARTICLE INFO

Article history:
Received 8 August 2017
Received in revised form 20 November 2017
Accepted 8 December 2017
Available online 12 December 2017

Keywords:
Magnetotelluric
Anisotropy
Three-dimensional
Forward modeling
Edge-based finite element method
Vector finite element method

ABSTRACT

It is important to understand how magnetotelluric (MT) modeling can most effectively be performed in general anisotropic media. However, previous studies in this area have mainly focused on the use of one-dimensional (1D) and two-dimensional (2D) algorithms. Thus, building on earlier work, it is important to study the performance of three-dimensional (3D) modeling in arbitrary conductivity media; therefore, an edge-based finite element (FE) method has been developed for 3D MT modeling in arbitrary conductivity media. This approach is based on the initial derivation of a series of equivalent variational equations that are based on Maxwell equations, generated using the weighted residual method. Specific values were then obtained for coefficient matrixes of this edge-based FE method using hexahedral meshes, and the algorithm was verified by comparing its results with finite difference (FD) solutions generated using a 2D anisotropic model. Finally, the results of a 3D anisotropic model were analyzed detailed for three conditions; another 3D anisotropic model was designed and its results were compared with two isotropic models'.

1. Introduction

The magnetotelluric (MT) method is an important geophysical method that has been widely used in many fields such as mineral resources survey, exploration of oil & gas and the investigation of deep Earth electrical structures. However, the interpretation of MT data generally assumes an isotropic medium, and numerous studies have shown that the Earth is anisotropic (Christensen, 1984; Wannamaker, 2005). A general ignorance about the influence of anisotropic media on MT has thus likely led to misinterpretations, which means that it is both important and meaningful to study the modeling and inversion of this approach in anisotropic media. Although approaches for the modeling and inversion of MT in one-dimensional (1D) and the modeling in two-dimensional (2D) anisotropic media are relatively mature, inversions in 2D and three-dimensional (3D) anisotropic media and the modeling in 3D anisotropic situations urgently need to be developed. A number of analytical solutions are available for 1D situations on the basis of numerous studies (O'Brien and Morrison, 1967; Reddy and Rankin, 1971; Dekker and Hastie, 1980; Yin, 2000; Pek and Santos, 2002), while the electrical and magnetic field cannot easily be separated in 2D cases. Nevertheless, a large number of studies have been carried out in this area (Heise and Pous, 2001, 2003; Yin, 2003; Hu et al., 2013; Huo et al., 2015); Pek and Verner (1997), for instance, developed a staggered-grid finite difference (FD) method for application in arbitrary 2D anisotropic media, which has had significant influence in the field. In later work, Li (2002) developed a modeling approach using the finite element (FD) method in 2D generally anisotropic media; the results of this research are in close agreement with solutions based on the FD method. Li and Pek (2008) subsequently developed an adaptive FE modeling algorithm in 2D general anisotropic media. In 3D anisotropic media, there are some studies of Marine Controlled-source Electromagnetic (Yin et al., 2014; Cai, et al., 2015). To date, however, just a handful of studies have applied MT modeling to 3D anisotropic media; one early example was the work of Martrinelli and Osella (1997) who presented a Rayleigh-Fourier method which allows for vertical anisotropy, while Weidelt (1999) later developed a staggered-grid FD method for use in 3D general anisotropic conductivity media that does not require a significant computational increase. Li (2000) presented a detailed nodal-based FE method for MT modeling, generating variational equations using the Galerkin weighted residual method, while Wang and Fang (2001) developed an FD algorithm for multicomponent electromagnetics in 3D anisotropic formations but did not present a case study example. Häuserer and Junge (2011) simulated a 3D anisotropic anomaly based on real data from Uganda, while Löwer and Junge (2017) studied the spatial and frequency-dependent behavior of phase tensors and tipper vectors using the FD method within an anomalous 3D anisotropic conductive body.

There are several serious problems inherent to the use of node-based elements within an FE model (Jin, 2002). Thus, a 3D MT

* Corresponding author.
E-mail address: 1052170058@qq.com (T. Xiao).

https://doi.org/10.1016/j.jappgeo.2017.12.009
0926-9851/

numerical modeling algorithm was implemented using an edge-based element method in arbitrary conductive media. The system of equations derived was a large, sparse matrix equation. It was solved using the bi-conjugate gradient-stabilized (Bi-CGSTAB) method combined with the symmetric successive over-relaxation (SSOR) preconditioner. The modeling method was validated comparing its calculation results with those obtained using FD method (Pek and Verner, 1997) for a 2D anisotropic model. The results of a 3D anisotropic model, a 3D anisotropic anomaly embedded in an isotropic half-space, were analyzed detailed for three conditions and some conclusions were obtained. At last, another 3D anisotropic combined model and two isotropic models were designed, the resistivities of the two special 3D isotropic model are the same as the resistivities of the anisotropic model in the x- and y-direction respectively. The results of this anisotropic model were compared with these two isotropic models'.

2. The modeling of MT in 3D anisotropic media

The study space utilized in this work is shown in Fig. 1, divided into air zone and subterranean zone. The sources are located on the top surface ABCD.

2.1. Differential equations

In the case of a quasi-stationary approximation, we consider a harmonic time dependence $e^{-i\omega t}$, and ignore displacement currents for MT. Thus, Maxwell's equations are changed, as follows:

$$\nabla \times \mathbf{E} = i\omega\mu\mathbf{H} \tag{2.1}$$

$$\nabla \times \mathbf{H} = \tilde{\sigma}\mathbf{E} \tag{2.2}$$

$$\nabla \cdot \mathbf{H} = 0 \tag{2.3}$$

$$\nabla \cdot \mathbf{E} = 0 \tag{2.4}$$

where $\mathbf{E}$ and $\mathbf{H}$ are the electric field and the magnetic field respectively, ω is the angular frequency, μ is the magnetic permeability of the media (considered in this case to be equal to the value in a vacuum, μ_0), and $\tilde{\sigma}$ is a tensor conductivity in anisotropic medium, as follows:

$$\tilde{\sigma} = \begin{pmatrix} \sigma_{xx} & \sigma_{xy} & \sigma_{xz} \\ \sigma_{yx} & \sigma_{yy} & \sigma_{yz} \\ \sigma_{zx} & \sigma_{zy} & \sigma_{zz} \end{pmatrix} \tag{2.5}$$

Two methods (Yin, 2000; Pek and Santos, 2002) are available to define the conductivity tensor, the latter of which is adopted in this paper.
The magnetic field $\mathbf{H}$ can be obtained from Eq. (2.1). Substituting it into Eq. (2.2) generates Eq. (2.6), as follows:

$$\nabla \times \nabla \times \mathbf{E} - i\omega\mu\tilde{\sigma}\mathbf{E} = 0 \tag{2.6}$$

2.2. Variational problem

We applied the Galerkin variant of the weighted residuals method (Xu, 1994) to generate the variational equation. This was done by first multiplying Eq. (2.6) by the variation in the electric field, $\delta\mathbf{E}$, and then integrating across the whole study space. At the same time, we utilized vector identity (Eq. (2.7)) and the divergence theorem (Eq. (2.8)):

$$\nabla \cdot (\mathbf{A} \times \mathbf{B}) = (\nabla \times \mathbf{A}) \cdot \mathbf{B} - \mathbf{A} \cdot (\nabla \times \mathbf{B}) \tag{2.7}$$

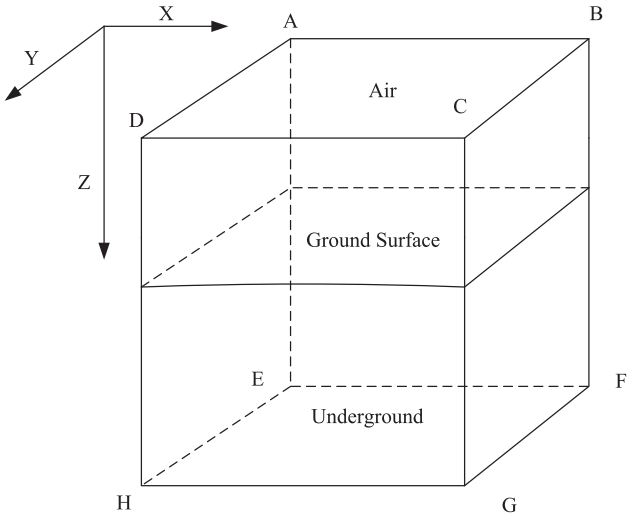

Fig. 1. The study space utilized for this research.

$$\int_v \nabla \cdot \mathbf{A} dv = \oint_\Gamma \mathbf{A} \cdot \mathbf{n} d\Gamma \tag{2.8}$$

Thus, we obtained Eq. (2.9), as follows:

$$\int_v \nabla \times \mathbf{E} \cdot \nabla \times \delta\mathbf{E} dv - i\omega\mu_0 \int_v \tilde{\sigma}\mathbf{E} \cdot \delta\mathbf{E} dv + \int_\Gamma \nabla \times \mathbf{E} \times \delta\mathbf{E} d\Gamma = 0 \tag{2.9}$$

We applied Dirichlet boundary condition (the first boundary condition) in this study for outer boundaries; in this case, the third integration of Eq. (2.9) equals zero. In the case of inner boundaries, the third integration of this equation still equals zero because of counteraction. Thus, Eq. (2.9) is reverted to Eq. (2.10) as follows:

$$\int_v \nabla \times \mathbf{E} \cdot \nabla \times \delta\mathbf{E} dv - i\omega\mu_0 \int_v \tilde{\sigma}\mathbf{E} \cdot \delta\mathbf{E} dv = 0 \tag{2.10}$$

2.3. An edge-based FE method

We adopted a Whitney vector as the basis for this study. Thus, taking into account the hexahedral elements shown in Fig. 2 that have side lengths denoted by a, b, and c in the x-, y-, and z-direction, the center coordinates are (x_0, y_0, z_0).

Thus, by assigning a tangential field component to each hexahedron edge, components within the element are expressed as follows:

$$\mathbf{E}_e = \sum_{i=1}^{4} \left(\mathbf{N}_e^{xi} E_e^{xi} + \mathbf{N}_e^{yi} E_e^{yi} + \mathbf{N}_e^{zi} E_e^{zi} \right) \tag{2.11}$$

where $\mathbf{N}_e^{xi}$, $\mathbf{N}_e^{yi}$ and $\mathbf{N}_e^{zi}$ are the basis (Jin, 2002).

Eq. (2.10) is also divided into constituent elements, as follows:

$$\sum_{n=1}^{n_e} \int_e \nabla \times \mathbf{E} \cdot \nabla \times \delta\mathbf{E} dv - \sum_{n=1}^{n_e} \int_e i\omega\mu_0 \tilde{\sigma}\mathbf{E} \cdot \delta\mathbf{E} dv = 0 \tag{2.12}$$

This process was then developed in two stages. In the first place, we analyzed the first integral of Eq. (2.12) for a given element, as follows:

$$\begin{aligned} \nabla \times \delta\mathbf{E} \cdot \nabla \times \mathbf{E} &= \nabla \times \sum_{i=1}^{4} \left(N_{xi} E_{xi} + N_{yi} E_{yi} + N_{zi} E_{zi} \right) \cdot \nabla \times \sum_{j=1}^{4} \left(N_{xj} E_{xj} + N_{yj} E_{yj} + N_{zj} E_{zj} \right) \\ &= \sum_{i=1}^{4} \sum_{j=1}^{4} \left\{ \left[\delta E_{xj} \;\; \delta E_{yj} \;\; \delta E_{zj} \right] \begin{bmatrix} \frac{\partial N_{xi}}{\partial y}\frac{\partial N_{xj}}{\partial y} + \frac{\partial N_{xi}}{\partial z}\frac{\partial N_{xj}}{\partial z} & -\frac{\partial N_{xi}}{\partial y}\frac{\partial N_{yj}}{\partial x} & -\frac{\partial N_{xi}}{\partial z}\frac{\partial N_{zj}}{\partial x} \\ -\frac{\partial N_{yi}}{\partial x}\frac{\partial N_{xj}}{\partial y} & \frac{\partial N_{yi}}{\partial x}\frac{\partial N_{yj}}{\partial x} + \frac{\partial N_{yi}}{\partial z}\frac{\partial N_{yj}}{\partial z} & -\frac{\partial N_{yi}}{\partial z}\frac{\partial N_{zj}}{\partial y} \\ -\frac{\partial N_{zi}}{\partial x}\frac{\partial N_{xj}}{\partial z} & -\frac{\partial N_{zi}}{\partial y}\frac{\partial N_{yj}}{\partial z} & \frac{\partial N_{zi}}{\partial x}\frac{\partial N_{zj}}{\partial x} + \frac{\partial N_{zi}}{\partial y}\frac{\partial N_{zj}}{\partial y} \end{bmatrix} \begin{bmatrix} E_{xi} \\ E_{yi} \\ E_{zi} \end{bmatrix} \right\} \end{aligned} \tag{2.13}$$

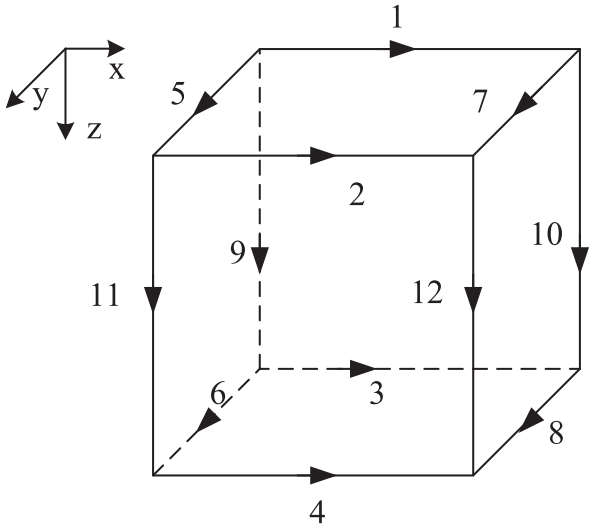

Fig. 2. Diagram of a hexahedral element.

The first integral of Eq. (2.12) over an element turns into the following:

$$\int_e \nabla \times \delta \mathbf{E} \cdot \nabla \times \mathbf{E} dv = \delta \mathbf{E}_e^T [K_{1e}] \mathbf{E}_e \tag{2.14}$$

Secondly, we analyzed the second integral of Eq. (2.12), as follows:

$$\begin{aligned} & i\omega\mu\tilde{\sigma}\mathbf{E} \cdot \delta\mathbf{E} \\ & = i\omega\mu \sum_{i=1}^{4}\sum_{j=1}^{4} \left\{ \begin{pmatrix} \delta E_{x,j} & \delta E_{y,j} & \delta E_{z,j} \end{pmatrix} \begin{pmatrix} \sigma_{xx} & \sigma_{xy} & \sigma_{xz} \\ \sigma_{yx} & \sigma_{yy} & \sigma_{yz} \\ \sigma_{zx} & \sigma_{zy} & \sigma_{zz} \end{pmatrix} \begin{pmatrix} N_{x,i}N_{x,j} & 0 & 0 \\ 0 & N_{y,i}N_{y,j} & 0 \\ 0 & 0 & N_{z,i}N_{z,j} \end{pmatrix} \begin{pmatrix} E_{x,i} \\ E_{y,i} \\ E_{z,i} \end{pmatrix} \right\} \end{aligned} \tag{2.15}$$

The second integral of Eq. (2.12) over an element turns into the following:

$$-\int_e i\omega\mu\tilde{\sigma}\mathbf{E} \cdot \delta\mathbf{E} dv = \delta \mathbf{E}_e^T [K_{2e}] \mathbf{E}_e \tag{2.16}$$

We then added Eqs. (2.14) and (2.16) and expand it to the whole space, as follows:

$$\delta\mathbf{E}^T \left[\sum_{n=1}^{n_e} \left(\overline{K_{1e}} + \overline{K_{2e}} \right) \right] \mathbf{E} = 0 \tag{2.17}$$

However, taking into account the fact that $\delta\mathbf{E}^T$ does not always equal zero as well as the imposition boundary conditions, the equation system is as follows:

$$[K]\mathbf{E} = [P] \tag{2.18}$$

where $[P]$ is composed of the last term of Eq. (2.17) and the Dirichlet boundary condition. Thus, after finally solving Eq. (2.18), electric field values were obtained.

2.4. Dirichlet boundaries

In this context, $S1$ and $S2$ are two orthogonal sources.

1) The source is located on the top surface (ABCD) and its initial value has no impact on the results, thus:

$$\mathbf{E}_{S1top} = (E_{S1x}, E_{S1y}, E_{S1z}) = (1,0,0), \mathbf{E}_{S2top} = (E_{S2x}, E_{S2y}, E_{S2z}) = (0,1,0) \tag{2.19}$$

2) In the case of the four side surfaces (ABFE, BCGF, CDHG, and ADHE), field values are obtained via 2D MT modeling.
3) We assume that the media below the bottom surface (EFGH) comprise an anisotropic half-space. Thus, values for $\mathbf{E}_x$ and $\mathbf{E}_y$ values can be obtained by linear interpolation.

3. Apparent resistivity and phase

We obtained the magnetic fields using Eq. (2.2), as follows:

$$H_x = \frac{1}{i\omega\mu_0}\left(\frac{\partial E_z}{\partial y} - \frac{\partial E_y}{\partial z}\right), \tag{3.1}$$

$$H_y = \frac{1}{i\omega\mu_0}\left(\frac{\partial E_x}{\partial z} - \frac{\partial E_z}{\partial x}\right), \tag{3.2}$$

and;

$$H_z = \frac{1}{i\omega\mu_0}\left(\frac{\partial E_y}{\partial x} - \frac{\partial E_x}{\partial y}\right). \tag{3.3}$$

Furthermore, the impedance tensor, apparent resistivities, and phases can be obtained (Li, 2002).

4. Numerical experiments

4.1. 2D anisotropic model

In order to test the adaption of the edge-based FE method in conductivity anisotropic media, the results of this algorithm for a 2D anisotropic model were compared with those obtained by the FD method (Pek and Verner, 1997). A 2D anisotropic model is presented in Fig. 3; this model has dimensions of 6000 m × 2900 m and a top depth of 1100 m, the 2D anomaly is embedded in an anisotropic half-space within this model; the three principal resistivities of this anomaly are 30 Ω·m, 10 Ω·m and 20 Ω·m, respectively, while the three Euler's

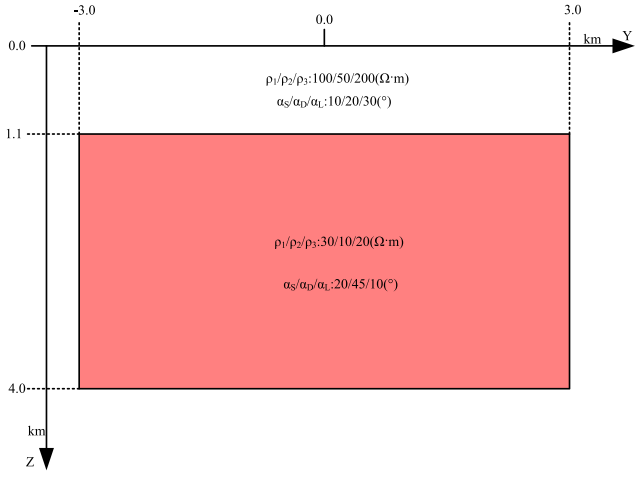

Fig. 3. The 2D anisotropic model.

angles are 20°, 45° and 10°, respectively. Similarly, the three principal resistivities of the anisotropic half-space are 100 Ω·m, 50 Ω·m and 200 Ω·m, respectively and the Euler's angles are 10°, 20° and 30°, respectively. Comparing apparent resistivities and phases with 10 Hz FD solutions (Fig. 4) reveals very close levels of agreement. The number of elements is 66,150 and the computational time is 1541 s. All the calculations in this paper were performed on a computer with Intel® Core ™ i7-4790 3.60 GHz processors, and a 64-bit Windows 7 operating system.

4.2. 3D anisotropic model 1

A 3D anisotropic anomaly is embedded in an isotropic half-space of 100 Ω·m (Fig. 5). The dimensions of this 3D anomaly are 2000 m × 2000 m × 1050 m, while the top depth is 240 m. At the same time, ρ_1 and ρ_2 are 1000 Ω·m and 10 Ω·m, respectively, while ρ_3 is 100 Ω·m, the same as the half-space. We studied these three cases respectively using a frequency of 0.1 Hz. The number of elements is 80,688 and the computational time for models in Sections 4.2.1 and 4.2.2 are all between 40 min and 60 min.

4.2.1. $\alpha_D = 0$, $\alpha_L = 0$ and α_S changes

The apparent resistivities of four modes with a different angle α_S (i.e., 0°, 30°, 60° and 90°) are shown in Fig. 6. The first row to the fourth row corresponding to the four modes (XX, XY, YX and YY) respectively, and the first column to the fourth column corresponding to α_S, which equals 0°, 30°, 60° and 90° respectively. Several symbols are used in this diagram: including a white square, which represents the location and shape of the 3D anomaly in the horizontal plane, and green solid lines, which represents the angles from left to right between them and the Y-direction at 0°, 30°, 60° and 90° respectively. At the same time, the purple solid lines from left to right represents the angles between them and X-direction at 0°, 30°, 60° and 90° respectively. The meanings of these symbols are held unchanged throughout this paper. The results of the first column and the fourth column show that the apparent resistivities of four modes all indicate clearly the anomaly location. In particular, when α_S equals 0° or 90°, the plane views well resolve the horizontal shape and size of the anomaly, and the plane views of apparent resistivities are symmetric with the x- and y-axis. In addition, analysis of the second row and the third row shows that the green solid lines agree well with the direction of the longer center lines of the red parts in the four subplots, and that purple lines agree well with the direction of the longer center lines of the blue parts. Therefore, the values of angle α_S can be reflected in the plane views of XY mode and YX mode apparent resistivities.

4.2.2. $\alpha_S = 0$, $\alpha_L = 0$ and α_D changes

The apparent resistivities of four modes with a different angle α_D (i.e., 0°, 30°, 60° and 90°) are shown in Fig. 7. The first row to the fourth row corresponds to the four modes (XX, XY, YX, and YY), and the first column to the fourth column corresponds to α_D equals 0°, 30°, 60° and 90° respectively. The results of the second row, the fourth row, and the first column all indicate well the horizontal location, size and shape of the 3D anomaly, while analysis of the second row and the fourth row reveals that the apparent resistivities of the XY mode and YY mode are almost unchanged when α_D changes. The further

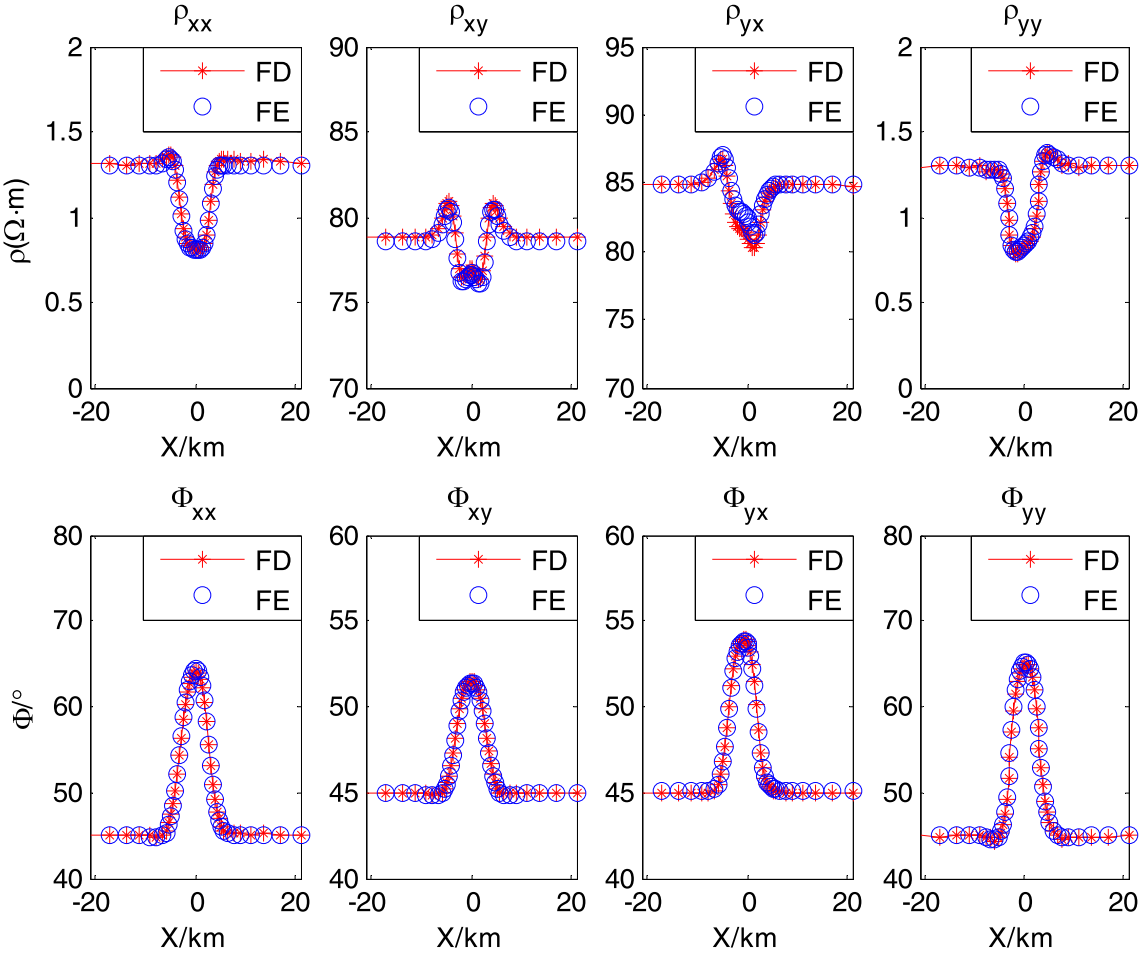

Fig. 4. The comparison of FE solutions and FD solutions.

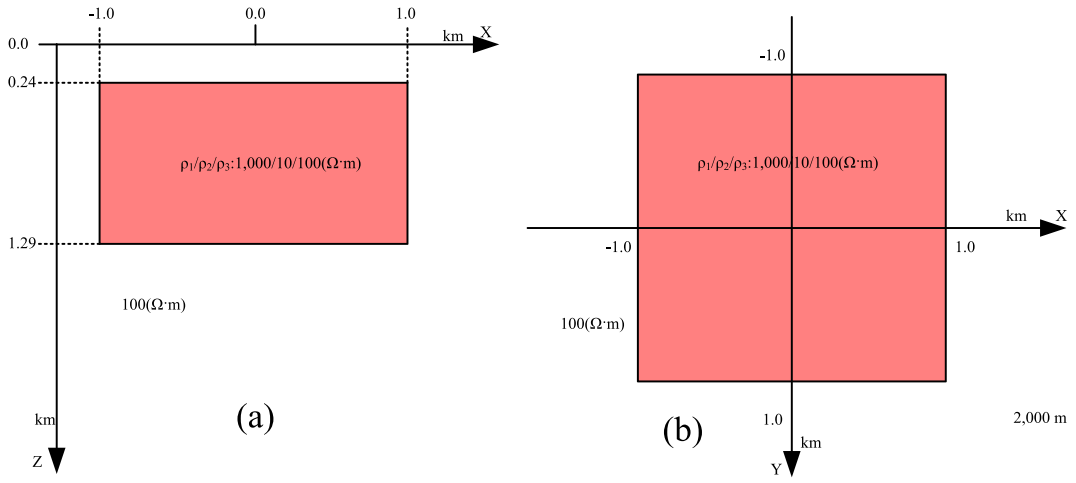

Fig. 5. The 3D anisotropic model: (a) Section view (left diagram); (b) Plan view (right diagram).

theoretical analysis shows that although the resistivities in the y- and z-direction change, those in the x-direction remain the same when α_D changes. We are therefore able to conclude that the XY mode and YY mode apparent resistivities are influenced mainly by resistivities in the x-direction. Furthermore, as X and Y are interchangeable, the XX and YX mode apparent resistivities are influenced mainly by resistivities in the y-direction. XX mode and YX mode apparent resistivities change when α_D changes. Therefore, on the basis of these results, we are able to conclude that resistivities in the z-direction almost have no influence to the apparent resistivities of the four modes. This conclusion is verified

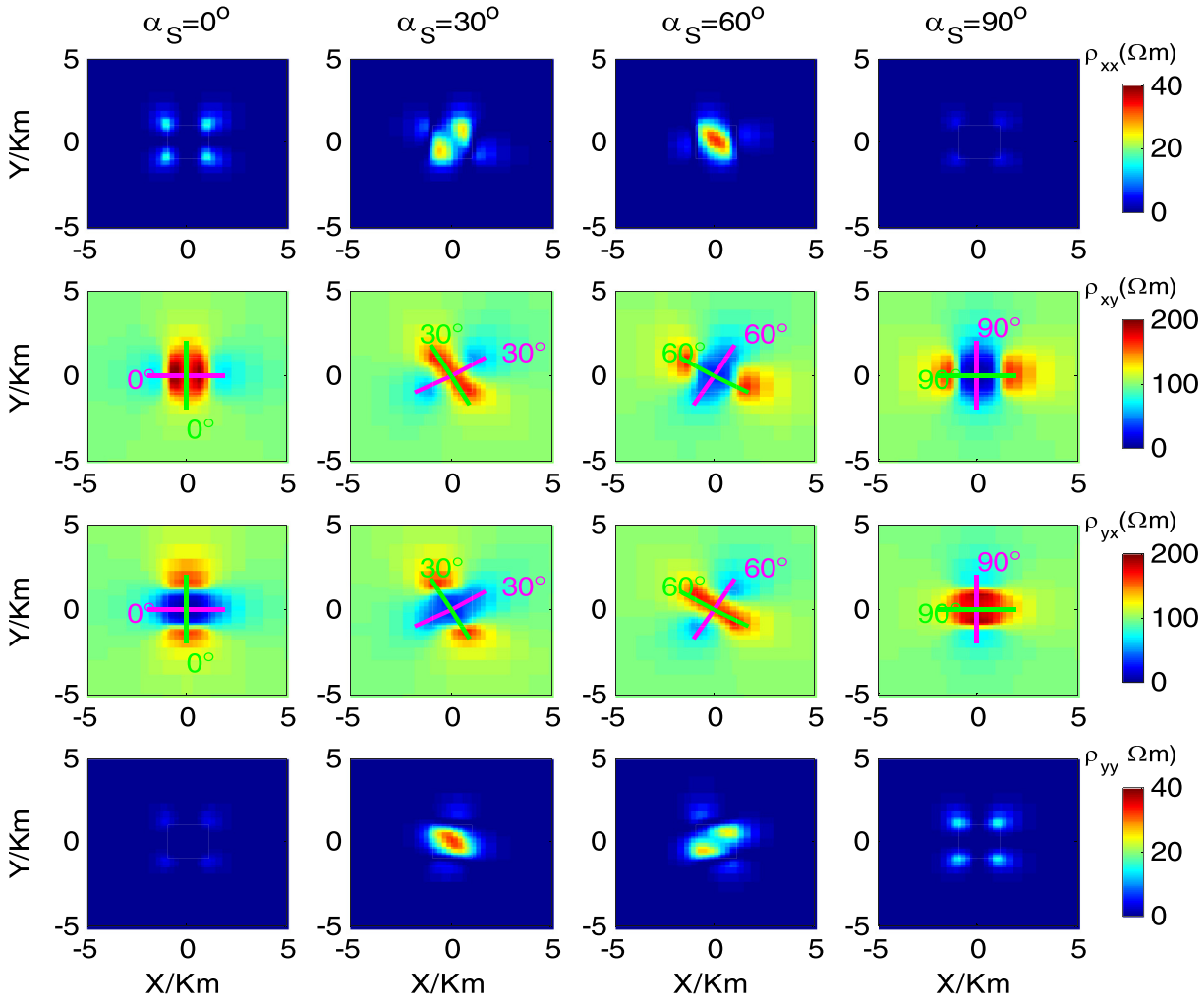

Fig. 6. Apparent resistivities with different angle α_S.

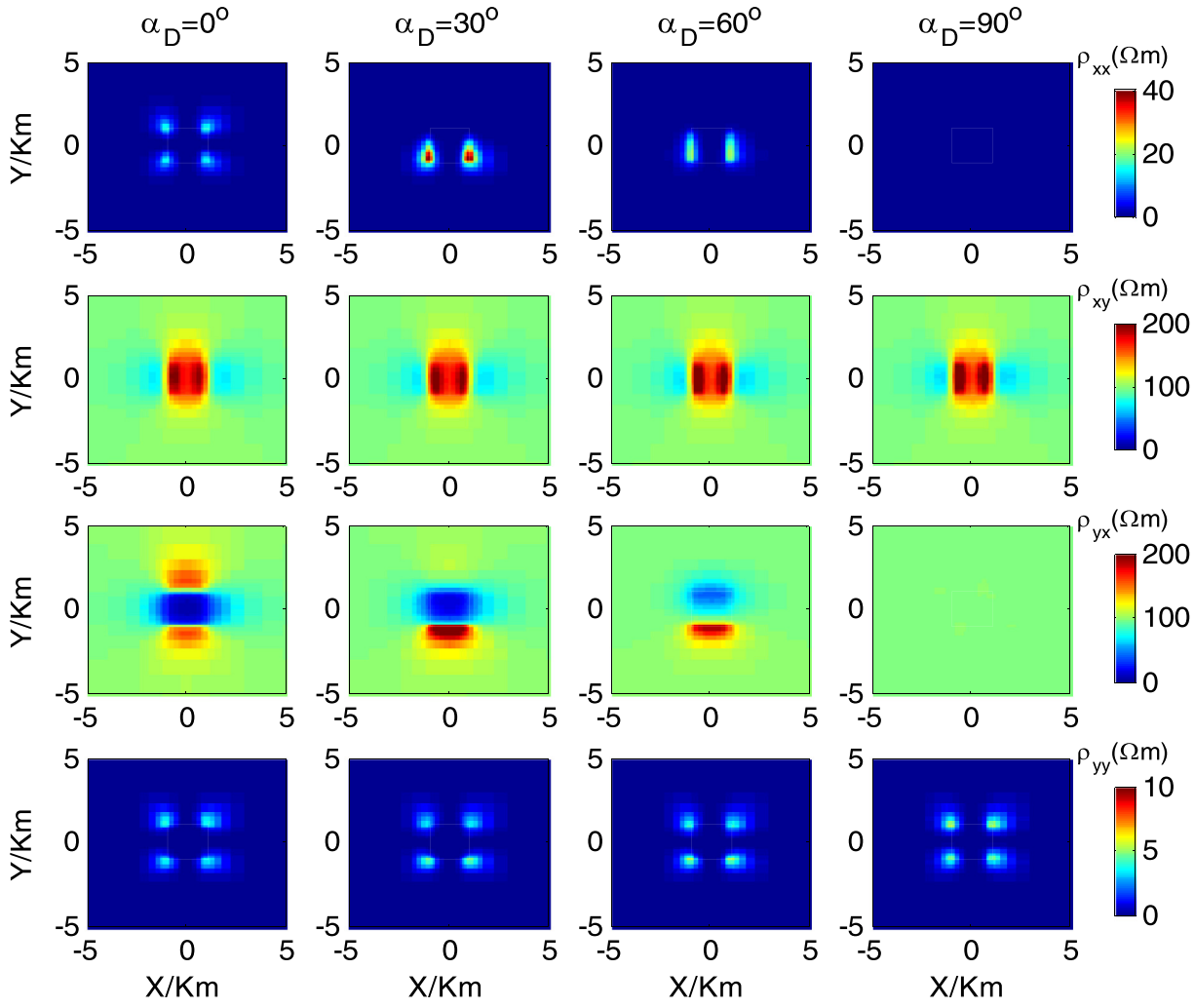

Fig. 7. Apparent resistivity with different α_D angles.

further below. Results also suggest that when α_D equals 90°, the XX mode and YX mode apparent resistivities show no anomaly. This is because when α_D equals 90°, ρ_2 and ρ_3 are exchanged, which leads to resistivities in Y-direction remaining unchanged; ρ_3 is 100 Ω·m, the same as the resistivity of the half-space. The result also verified the appropriateness of the algorithm used in this study. Results also show that when α_D equals 30° or 90°, plane views of both XX mode and YX mode apparent resistivities are symmetrical with the x-axis. Finally, effective information of α_D is not shown in resistivities plane views.

In order to verify the conclusion that resistivity in z-direction almost does not affect the apparent resistivities of the four modes, we applied the model in Section 4.2.1 but instead ρ_3 (100 Ω·m) with 50 Ω·m. The computed results with different α_S (i.e., 0°, 30°,60° and 90°) are almost the same as in Fig. 6, which again verified the conclusion.

4.2.3. $\alpha_S = 0$, $\alpha_D = 0$ and α_L changes

In this case, the results are the same as those shown in Section 4.2.1 and corroborate theoretical expectations. Results are not re-presented here.

4.3. 3D anisotropic model 2

An additional 3D anisotropic model is presented in Fig. 8; this model includes a 3D anisotropic anomaly and two 3D isotropic anomalies embedded in a half-space of 100 Ω·m. The three principal resistivities of this 3D anisotropic anomaly (the red block) are 1000 Ω·m, 10 Ω·m, and 100 Ω·m respectively, while the three Euler angles are all equal 0°. Besides, the resistivities of the two isotropic anomalies, the green block and the blue block, are 10 Ω·m and 1000 Ω·m respectively. The frequency computed is 0.1 Hz. The number of elements is 90,972 and the computational time for the three models are 3206 s, 3180 s and 2932 s respectively.

Fig. 9 shows the apparent resistivities of this model and those of two isotropic models, of which the anisotropic block is set to be an isotropic block of 1000 Ω·m (Isotropy 1 model) and 10 Ω·m (Isotropy 2 model) respectively. The three white rectangles in these figures mark the location and shape of the three anomalies in the horizontal plane. The first row to the fourth row corresponds to the four modes (XX, XY, YX, and YY), and the first column to the third column corresponds to Isotropy 1 model, Anisotropy model and Isotropy 2 model respectively. The results of the second row and the third row both indicate well the anomaly location and shape. Besides, ρ_{xx} and ρ_{yx} of the Isotropy 2 model are almost the same as ρ_{xx} and ρ_{yx} of the Anisotropy model, respectively; ρ_{xy} and ρ_{yy} of the Isotropy 1 model are very similar to ρ_{xy} and ρ_{yy} of the Anisotropy model, respectively. The further theoretical analysis shows that the resistivities of Isotropy 2 model are the same as the resistivities of Anisotropy model in the y-direction, and the resistivities of Isotropy 1model are the same as the resistivities of Anisotropy model in the x-direction. It is consistent with the conclusion in Section 4.2.2.

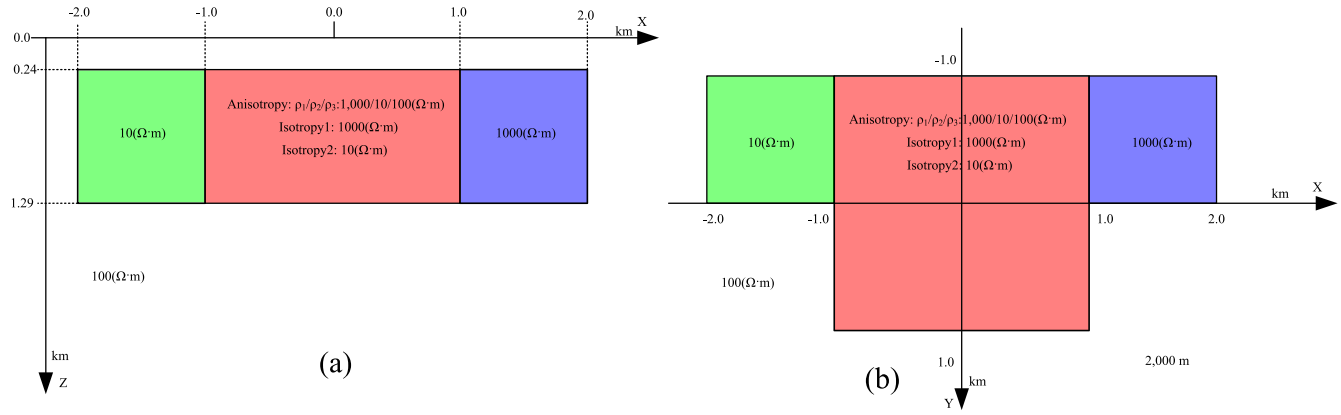

Fig. 8. 3D model 2: (a) Section view (left); (b) Plan view (right).

5. Conclusions

A 3D MT numerical modeling algorithm in arbitrary conductive was implemented using an edge-based element method. Comparisons with FD solutions for a 2D anisotropic model confirm the accuracy of our algorithm. Also studied the apparent resistivities of a simple 3D anisotropic model in three different conditions; compared the results of a combined 3D anisotropic model with two isotropic models, and

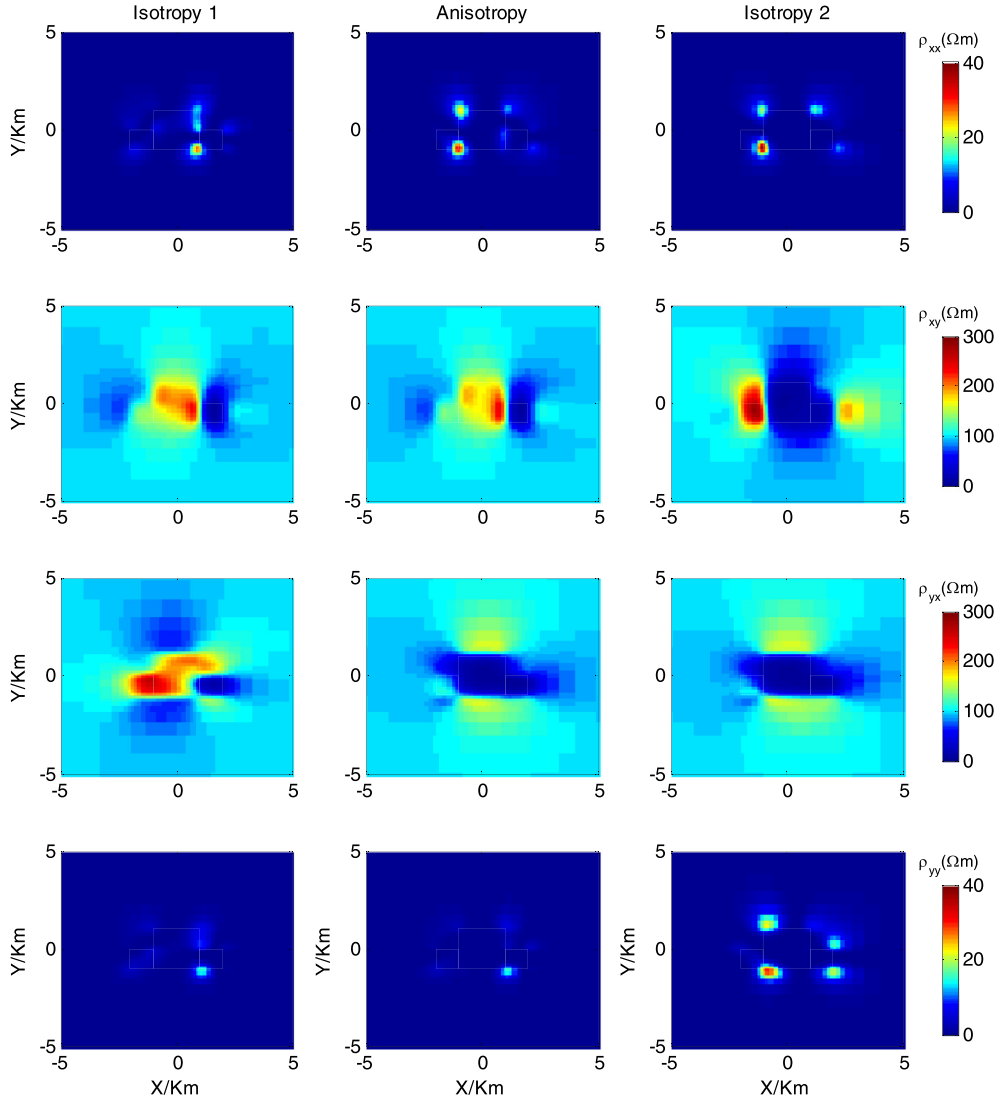

Fig. 9. Apparent resistivities of four modes for these three models.

presented four main conclusions. First, when α_S is not zero and the other two Euler angles do equal zero, plane views of apparent resistivity plane well reflect α_S information, as the same is true of α_L. Second, the apparent resistivities of both XY mode and YY mode are influenced mainly by resistivities in the x-direction. Third, XX mode and YX mode apparent resistivities are mainly influenced by resistivities in the y-direction, while fourth, resistivities in the z-direction almost have no impact on the apparent resistivities of the four modes.

Acknowledgements

This research is co-funded by the National Key Research and Development Project of China (2016YFC0600301), the National Natural Science Foundation of China (No. 41425017) and the National Key Research and Development Program of China (2016YFC0600505).

Appendix A. The values of $\mathbf{K}_{1e}$ and $\mathbf{K}_{2e}$

1) $\mathbf{K}_{1e}$

$$\mathbf{K}_{1e}=\begin{pmatrix}\mathbf{K}_{1e}^{xx} & \mathbf{K}_{1e}^{xy} & \mathbf{K}_{1e}^{xz}\\ \mathbf{K}_{1e}^{yx} & \mathbf{K}_{1e}^{yy} & \mathbf{K}_{1e}^{yz}\\ \mathbf{K}_{1e}^{zx} & \mathbf{K}_{1e}^{zy} & \mathbf{K}_{1e}^{zz}\end{pmatrix}$$

where

$$\tilde{\boldsymbol{\sigma}}^{-1}=\begin{pmatrix}\sigma_{inv}^{xx} & \sigma_{inv}^{xy} & \sigma_{inv}^{xz}\\ \sigma_{inv}^{yx} & \sigma_{inv}^{yy} & \sigma_{inv}^{yz}\\ \sigma_{inv}^{zx} & \sigma_{inv}^{zy} & \sigma_{inv}^{zz}\end{pmatrix}$$

$$K_{1e}^{xx}=\frac{ac}{6b}\begin{bmatrix}2&-2&1&-1\\-2&2&-1&1\\1&-1&2&-2\\-1&1&-2&2\end{bmatrix}+\frac{ab}{6c}\begin{bmatrix}2&1&-2&-1\\1&2&-1&-2\\-2&-1&2&1\\-1&-2&1&2\end{bmatrix},$$

$$K_{1e}^{xy}=-\frac{c}{6}\begin{bmatrix}2&1&-2&-1\\-2&-1&2&1\\1&2&-1&-2\\-1&-2&1&2\end{bmatrix},$$

$$K_{1e}^{xz}=-\frac{b}{6}\begin{bmatrix}2&-2&1&-1\\1&-1&2&-2\\-2&2&-1&1\\-1&1&-2&2\end{bmatrix},$$

$$K_{1e}^{yx}=-\frac{c}{6}\begin{bmatrix}2&-2&1&-1\\1&-1&2&-2\\-2&2&-1&1\\-1&1&-2&2\end{bmatrix},$$

$$K_{1e}^{yy}=\frac{bc}{6a}\begin{bmatrix}2&1&-2&-1\\1&2&-1&-2\\-2&-1&2&1\\-1&-2&1&2\end{bmatrix}+\frac{ab}{6c}\begin{bmatrix}2&-2&1&-1\\-2&2&-1&1\\1&-1&2&-2\\-1&1&-2&2\end{bmatrix},$$

$$K_{1e}^{yz}=-\frac{a}{6}\begin{bmatrix}2&1&-2&-1\\-2&-1&2&1\\1&2&-1&-2\\-1&-2&1&2\end{bmatrix},$$

$$K_{1e}^{zx}=-\frac{b}{6}\begin{bmatrix}2&1&-2&-1\\-2&-1&2&1\\1&2&-1&-2\\-1&-2&1&2\end{bmatrix},$$

$$K_{1e}^{zy}=-\frac{a}{6}\begin{bmatrix}2&-2&1&-1\\1&-1&2&-2\\-2&2&-1&1\\-1&1&-2&2\end{bmatrix},$$

$$K_{1e}^{zz}=\frac{bc}{6a}\begin{bmatrix}2&-2&1&-1\\-2&2&-1&1\\1&-1&2&-2\\-1&1&-2&2\end{bmatrix}+\frac{ac}{6b}\begin{bmatrix}2&1&-2&-1\\1&2&-1&-2\\-2&-1&2&1\\-1&-2&1&2\end{bmatrix}$$

2) $\mathbf{K}_{2e}$

$$\mathbf{K}_{2e}=\begin{pmatrix}\mathbf{K}_{2e}^{xx} & \mathbf{0} & \mathbf{0}\\ \mathbf{0} & \mathbf{K}_{2e}^{yy} & \mathbf{0}\\ \mathbf{0} & \mathbf{0} & \mathbf{K}_{2e}^{zz}\end{pmatrix}$$

where

$$\mathbf{K}_{2e}^{xx}=\mathbf{K}_{2e}^{yy}=\mathbf{K}_{2e}^{zz}=-i\omega\mu\frac{abc}{36}\begin{pmatrix}4&2&2&1\\2&4&1&2\\2&1&4&2\\1&2&2&4\end{pmatrix}$$

References

Cai, H.Z., Xiong, B., Zhdanov, Michael, 2015. Three-dimensional marine controlled-source electromagnetic modeling in anisotropic medium using finite element method. Chin. J. Geophys. 58 (8), 2839–2850 (in Chinese).
Christensen, N.I., 1984. The magnitude, symmetry and origin of upper mantle anisotropy based on fabric analyses of ultramafic tectonites [J]. Geophys. J. R. Astron. Soc. 76 (1), 89–111.
Dekker, D.L., Hastie, L.M., 1980. Magneto-telluric impedances of an anisotropic layered Earth model [J]. Geophys. J. R. 61, 11–20.
Häuserer, Michael, Junge, Andreas, 2011. Electrical mantle anisotropy and crustal conductor: a 3-D conductivity model of the Rwenzori region in western Uganda. Geophys. J. Int. 185, 1235–1242.
Heise, Wiebke, Pous, Jaume, 2001. Effects of anisotropic on the two-dimensional inversion procedure. Geophys. J. Int. 147, 610–621.
Heise, Wiebke, Pous, Jaume, 2003. Anomalous phases exceeding 90° in magnetotellurics: anisotropic model studies and a field example. Geophys. J. Int. 155, 308–318.
Hu, X.Y., Huo, G.P., Gao, R., et al., 2013. The magnetotelluric anisotropic two-dimensional simulation and case analysis. Chin. J. Geophys. 56 (12), 4268–4277 (in Chinese).
Huo, G.P., Hu, X.Y., Huang, Y.F., et al., 2015. MT modeling for two-dimensional anisotropic conductivity structure with topography and examples of comparative analyses. Chin. J. Geophys. 58 (12), 4696–4708 (in Chinese).
Jin, J.M., 2002. The Finite Element Method In Electromagnetics. 2nd ed. John Wiley & Sons.
Li, Y., 2000. Finite Element Modeling of Electromagnetic Fields in Two-and Three-dimensional Anisotropic Conductivity Structures. (Doctoral Thesis). University of Gottingen.
Li, Y., 2002. A finite element algorithm for electromagnetic induction in two dimensional anisotropic conductivity structures. Geophysics 148, 389–401.
Li, Y., Pek, J., 2008. Adaptive finite element modelling of two-dimensional magnetotelluric fields in general anisotropic media. Geophys. J. Int. 175, 942–954.
Löwer, Alexander, Junge, Andreas, 2017. Magnetotelluric transfer functions: phase tensor and tipper vector above a simple anisotropic three-dimensional conductivity anomaly and implications for 3D isotropic inversion. Pure Appl. Geophys. 174, 2089–2101.
Martrinelli, Patricia, Osella, Ana, 1997. MT forward modeling of 3-D anisotropic electrical conductivity structures using the Rayleigh-Fourier method. J. Geomag. Geolectr. 49, 1499–1518.
O'Brien, D.P., Morrison, H.F., 1967. Electromagnetic fields in an N-layered anisotropic half-space [J]. Geophysics 32 (4), 668–677.
Pek, J., Santos, F.A.M., 2002. Magnetotelluric impedances and parametric sensitivities for 1-D anisotropic layered media. Comput. Geosci. 28, 935–950.
Pek, Josef, Verner, Tomáš, 1997. Finite-difference modelling of magnetotelluric fields in two-dimensional anisotropic media. Geophys. J. Int. 128, 505–521.
Reddy, I.K., Rankin, D., 1971. Magnetotelluric effect of dipping anisotropies [J]. Geophys. Prospect. 19 (1), 84–97.
Wang, Tsili, Fang, Sheng, 2001. 3-D electromagnetic anisotropy modeling using finite differences. Geophysics 66 (5), 1386–1398.
Wannamaker, P.E., 2005. Anisotropy versus heterogeneity in continental solid earth electromagnetic studies: fundamental response characteristics and implications for physicochemical state [J]. Surv. Geophys. 26 (6), 733–765.
Weidelt, Peter, 1999. 3-D conductivity models: implications of electrical anisotropy. Three-Dimensional Electromagnetics 7, 119–137.
Xu, Shizhe, 1994. The Finite Element Methods in Geophysics. (in Chinese). Science Press.
Yin, Changchun, 2000. Geoelectrical inversion for a one-dimensional anisotropic model and inherent non-uniqueness [J]. Geophys. J. Int. 140 (1), 11–23.
Yin, C., 2003. Inherent nonuniqueness in magnetotelluric inversion for 1D anisotropic models. Geophysics 68 (1), 138–146.
Yin, C.C., Ben, F., Liu, Y.H., et al., 2014. MCSEM 3D modeling for arbitrary anisotropic media. Chin. J. Geophys. 57 (12), 4110–4122 (in Chinese).